Robust solid electrolyte interphases in localized high concentration electrolytes boosting black phosphorus anode for K-ion batteries

*Xiaoqiong Du, Biao Zhang**

Department of Applied Physics, The Hong Kong Polytechnic University, Hung Hom, Hong Kong, China.

*Corresponding Author. E-mail address: biao.ap.zhang@polyu.edu.hk (Biao Zhang)

ABSTRACT

Black phosphorous (BP) shows superior capacity towards K-ion storage, yet it suffers from poor reversibility and fast capacity degradation. Herein, BP-graphite (BP/G) composite with a high BP loading of 80 wt.% is synthesized and stabilized *via* the utilization of a localized high concentration electrolyte (LHCE), *i.e.*, KFSI in trimethyl phosphate (TMP) with a fluorinated ether as the diluent. We reveal the benefits of high concentration electrolytes rely on the formation of inorganic component rich solid electrolyte interphase (SEI), which effectively passivate the electrode from copious parasite reactions. Furthermore, the diluent increases the electrolyte's ionic conductivity for achieving attractive rate capability and homogenizes the element distribution in the SEI. The latter essentially improves SEI's maximum elastic deformation energy for accommodating the volume change, resulting in excellent cyclic performance. This work promotes the application of advanced K-ion batteries by adopting high-capacity BP anodes, on the one hand. On the other hand, it unravels the beneficial roles of LHCE in building robust SEI for stabilizing alloy anodes.

KEYWORDS

black phosphorous; solid electrolyte interphase; K-ion batteries, localized high concentration electrolyte; atomic force microscopy.

Introduction

K-ion batteries (KIBs) have become an attractive energy storage system in recent years owing to the abundant K resources.[1-2] Moreover, the smaller Stokes radius of solvated K and lower standard redox potential of K^+/K than Na/Li counterparts in non-aqueous electrolytes promise fast ion transport and high operation voltages.[3] Various anode materials have been explored for K ion storage, centering mainly on carbonaceous materials,[4-6] alloys,[7-9] metal oxides/sulfides/selenides,[10-12] and phosphorus-based materials.[13-15] Among these, phosphorous (P) has been predicted to be one of the highest-capacity anodes for alloying up to 1.33 K ion per P atom, corresponding to 1154 mAh g^{-1} capacity.[16] Three types of P allotropes exist in nature, *i.e.*, red phosphorous (RP), white phosphorous (WP), and black phosphorous (BP).[17] WP is precluded as a potential anode because of the safety issues associated with the self-ignition under ambient temperature. The non-toxic and safe RP is widely studied as anode materials for alkali metal ion storage.[18-22] However, the poor electronic conductivity and large volume expansion (301% for forming K_4P_3) hinder its development in KIBs. The low electronic conductivity of $\sim10^{-14}$ S cm^{-1} makes bare RP hardly directly employed as electrodes.[23] The combination with conductive carbon is an effective strategy to modify its intrinsic poor electronic conductivity.[24-26] Taking advantage of low sublimation temperature (~419˚C), the RP could be encapsulated into the pores of carbon materials through a vaporization condensation conversion method, which enhances the conductivity and buffers the large volume change of P in the carbon matrix.[27-28] The drawback is that WP will be produced during condensation. Thus, the composites need to be washed by toxic carbon disulfide (CS_2) solvent to remove WP residual.[29] Besides, the large specific surface area of the carbon host will cause severe electrolyte decompositions in the first cycle with a low initial Coulombic efficiency (ICE).

BP is a two-dimensional layered material with an interlayer distance of 5.2 Å. It possesses the best thermal stability and electronic conductivity of $0.2\text{-}3.3\times10^{2}$ S cm^{-1} among all the P allotropes.[30] Chemical vapor deposition (CVD) is extensively used to synthesize BP with superior crystallinity, but the high cost and low BP yielding of CVD discourage the wide application in the battery.[31-32] Mechanical ball milling is recognized as a practical approach to fabricate BP and its composite with carbon (BP/C) at a large scale.[33-34] Unfortunately, due to the difficulties in controlling the morphologies during ball milling, the particle size is relatively large and non-uniform, ranging from hundreds of nanometers to tens of micrometers.[35] Although the large particles reduce the active surface with electrolytes and benefit the high ICE, the ball-milled BP/C composites usually show rapid capacity decay in KIBs because of the particle pulverization during cycling.[36-38]

High concentration electrolytes (HCE, usually > 3M) show promising potentials in improving the cyclic stabilities of anode materials,[39-41] attributing to the interfacial chemistry induced by compressed solvation sheaths.[42] The modified ion solvation structures help build a salt anion-derived solid electrolyte interphase (SEI) to suppress continuous electrolyte decompositions.[43] To resolve the high viscosity of HCE, a localized high concentration electrolyte (LHCE) is proposed and has been popularly adopted in Li/Na batteries.[44-48]. Such a LHCE relies on fluorinated ethers as nonsolvent to dilute the HCE without changing its ion solvation structures.[49] The LHCEs are rarely researched for KIBs, probably due to the phase separation of fluorinated ethers and carbonate solvents in high concentration K electrolytes, although it is not a problem in Li electrolytes.[50-51] Recently, Qin *et al*. reported a LHCE based on KFSI/monoglyme (DME) system, which enables excellent cyclability of graphite anode by toughening the SEI on graphite,[52] but the direct extension to alloy anodes has not been successful. In this work, we deviate from DME solvent and focus on trimethyl phosphate (TMP)-based electrolytes considering its non-flammability with a high flash point of 150˚C (compared to 5˚C for DME). It also possesses excellent oxidative stability to be compatible with high-voltage cathodes for practical applications. Furthermore, the high dielectric constant of 21.6 allows the preparation of highly concentrated electrolytes up to 6.6 M with KFSI salt.[53-54] We demonstrate that LHCE based on KFSI/TMP system with a 1,1,2,2-tetrafluoroethyl-2,2,2-trifluoroethyl ether (HFE) diluent realizes the stable cycling of BP-graphite (BP/G) anode with a high BP loading of 80 wt.%. The BP/G electrodes show high reversible capacities of 618 mAh g^{-1} under 0.1 A g^{-1} and outstanding long-term cyclic stability with 342 mAh g^{-1} after 300 cycles under 0.3 A g^{-1} in LHCE.

Results and Discussion

Commercial RP is purified by washing in boiling water, which is adopted to synthesize BP through high-energy ball milling (HEBM). The X-ray diffraction (XRD) in Figure 1a shows that the purified RP presents a medium-range order structure as manifested by the broad peak at about 15˚ and confirmed in transmission electron microscopy (TEM, Figure S1).[55] RP is completely transformed to rhombohedral BP (PDF#73-1358) after HEBM. Raman spectra also identify the successful synthesis of BP. The Raman peaks at 347, 381-405, and 462 cm^{-1} (Figure 1b) match B_1

(fundamental mode), A_1 (symmetric stretch mode) and E_1 (degenerate mode) vibrations in RP.[56] In comparison, there are three peaks at 362, 434, and 462 cm^{-1} after ball milling, corresponding to A_g^1 (out-of-plane mode), B_{2g}, and A_g^2 (in-plane mode) of BP, respectively.[57] The BP exhibits a large particle size up to several micrometers (Figure 1c). The d-spacing of 0.52 nm in high-resolution TEM (HRTEM) is indexed to the (202) plane of BP. The BP is further mixed with graphite to prepare a BP/G composite through planetary ball milling for increasing the electronic conductivity and potentially forming a P-C bond as will be discussed later. There are no sharp peaks except two humps at about 23° and 35° in the XRD pattern of BP/G, indicating the long-term ball milling decreases the crystallinity of the BP. In the Raman spectrum of BP/G composite, the BP peaks between 350-500 cm^{-1} become invisible, and only the D (1340 cm^{-1}) and G (1586 cm^{-1}) bands of graphite are detected. The D band originates from A_{1g} ring breathing mode, which is absent in perfect graphite, and G band arises from E_{2g} vibration mode of sp^2 carbon atoms.[58] The increase of D band (I_D/I_G=1.04) implies that significant defects are introduced in BP/G composite. The morphologies of BP/G composite are examined by TEM and scanning electron microscope (SEM) (Figure 1d, Figure S10a and b). It maintains the microparticle characteristic and exhibits the uniform elemental distribution of P and C in EDS mappings (Figure S2). Moreover, the chemical structures of BP/G are studied by X-ray photoelectron spectroscopy (XPS). As shown in Figure S3, P-C bonding is found in both C1s (283.5 eV) and P2p spectra (130.3 eV), which would help reduce the energy barriers of ion migrations for fast alloying reactions.[26, 59]

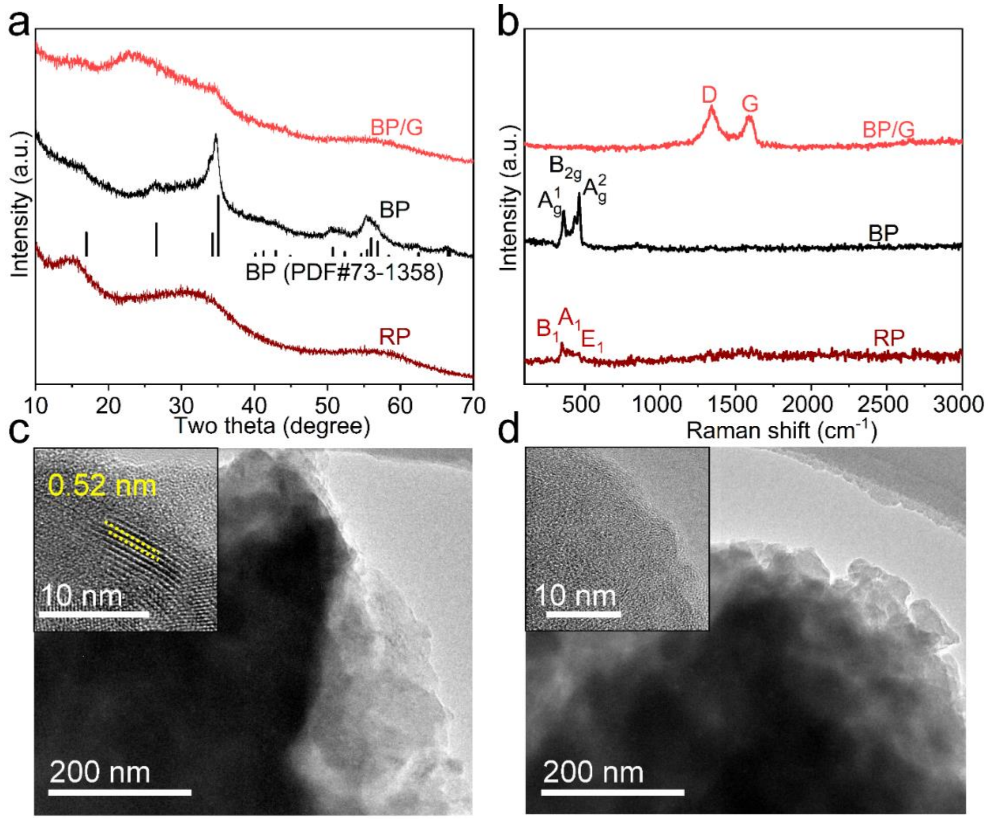

Figure 1 Sample preparation. a) XRD patterns and b) Raman spectra of RP, BP, and BP/G composite; TEM images of (c) BP and (d) BP/G composite.

Three alkylphosphates electrolytes with different formulations are prepared for examining the electrochemical performance of BP/G, namely NCE (1M KFSI/TMP), HCE (5M KFSI/TMP), and LHCE (KFSI/TMP/HFE=1:1.7:2 by mol.). The ionic conductivities of the electrolytes are compared in Figure S4. Increasing the concentration reduces the ionic conductivity from 5.31 for NCE to 1.82 mS cm^{-1} for HCE because of the increased ion-pairing.[60] After adding HFE diluent in LHCE, the value is enhanced to 3.08 mS cm^{-1}. The solvation structures of the electrolytes are investigated by Raman spectroscopy. In Figure 2a, two distinct peaks at 737 and 751 cm^{-1} are presented in TMP solvent, which can be ascribed to asymmetric P-O-C stretching of free TMP molecular.[54] The free stretching peaks persist in NCE, although the intensity is weakened. In contrast, they are disappeared in HCE and LHCE, implying that all TMP molecules participate in

K solvation in high concentration electrolytes.[43] In Figure 2b, a prominent peak at 1216 cm^{-1} is observed in NCE, which comes from the S=O stretching in FSI^- anion. This peak shifts to the high frequency of 1221 cm^{-1} in HCE and LHCE owing to the enhanced coordination between K^+ and FSI^-. Besides, the vibration band of HFE between 840-870 cm^{-1} does not show apparent shifts in LHCE (Figure S5) since HFE molecules have minimal interaction with K ions.[61]

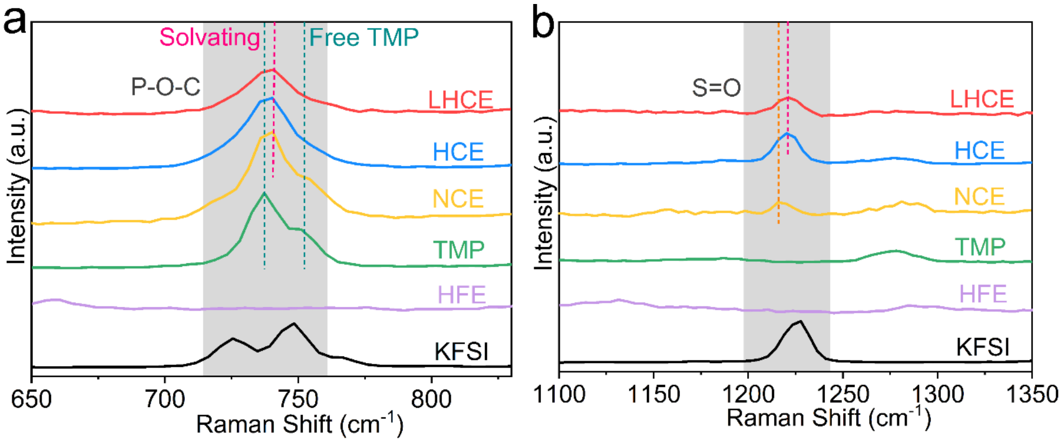

Figure 2 Electrolyte solvation structures. a) and b) Raman spectra of NCE, HCE, LHCE, KFSI, TMP and HFE.

The cyclic voltammetry (CV) curves are first scrutinized to study the faradaic response of BP/G electrodes in the electrolytes mentioned above (Figure 3a). A broad peak at 0.5-1.2 V is shown in the first cycle under all the electrolytes due to the formation of SEI. In NCE, the CV curves do not reveal evident peaks after the first cycle as a reflection of the poor reversibility of the electrode. As for HCE and LHCE, two pronounced reduction peaks at 0.8-1.0 V and 0.25-0.27 V are observed in the cathodic sweep, which is associated with the formation of K_xP ($x<1.33$) and K_4P_3, respectively.[62] Correspondingly, two oxidation peaks at about 0.8 V and 1.7 V appear in anodic scan due to the reversible de-alloying process. Raman spectroscopy is then performed to elucidate the K ion storage mechanisms of BP/G composite. No distinct peak, except for graphite peaks, is detected at a fully discharged state in NCE, while three Raman peaks at 392, 474, and 950 cm^{-1}

emerge in HCE (Figure S6a and b). Combined with the CV curves in NCE and HCE, it can decipher that the BP/G composite is not alloyed with K in NCE but reacts successfully in HCE and LHCE. The *ex situ* Raman spectra for LHCE are shown in Figure 3b. In the state of discharging to 0.8V, a broad peak at about 440 cm^{-1} is found, possibly relating to the formation of KP_2.[63] When discharging from 0.2 V to 0V, three distinct peaks in similar positions as those in HCE show high intensities, which is supposed to be K_4P_3 phase.[62] To confirm the final potassiated products, the K_4P_3 is chemically synthesized by HEBM using K metal and BP powder with a stoichiometric ratio of 4:3. As observed in Figure S7, a group of K_4P_3 peaks is well-defined, consistent with the peaks at a fully discharged state. Upon charge (Figure 3b), the sharp peak at 473 cm^{-1} is disappeared and turns to a weak peak after charging to 1.0 V. Broad peaks located at between 350 and 500 cm^{-1} arise when charging to above 1.8 V, evidencing the potassiated phases recovered to BP (Figure S8). Similarly, the BP peaks are detected when charging back to 2.5 V in HCE electrolyte as well (Figure S6b). The observations demonstrate the highly reversible alloying and de-alloying processes of $4K+3P \leftrightarrow K_4P_3$ in high concentration electrolytes.

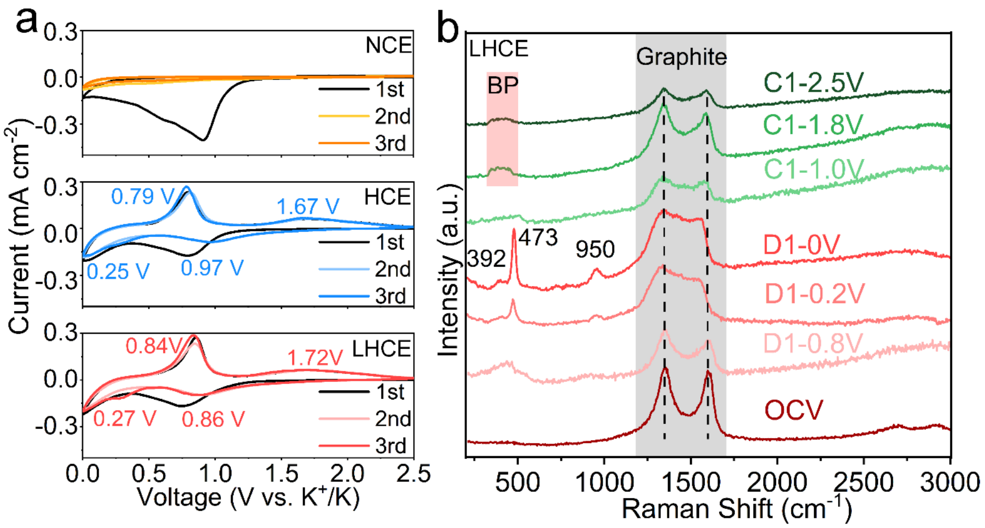

Figure 3 a) CV curves of BP/G electrodes in NCE, HCE and LHCE at the scan rate of 0.1 mV s^{-1}; b) *Ex situ* Raman characterization of BP/G electrodes under different states in LHCE (note: D1-0.8V represents 0.8V in the first discharge process).

The electrochemical performances of BP/G composite in KIBs are evaluated in coin cells, and the specific capacities are calculated based on the total mass of BP/G composite. As shown in Figure S9a, the BP/G electrode shows a large discharge capacity and minor charge capacity with an extremely low ICE of 3.7% in NCE. We speculate that the electrolyte decomposition dominates the process owing to the failure of forming an effective protective SEI layer. As observed in SEM images (Figure S10), a thick layer consisting of electrolyte reduction products is coated on the electrode's surface after only three cycles in NCE, compared to the neat electrode surface under HCE and LHCE. The restricted alloy reaction is also evidenced by the absence of K_xP phases in the Raman spectra since nearly all the discharge capacity arises from electrolyte reduction (Figure S6a). In sharp contrast, a high reversible capacity of 536 mAh g^{-1} with ICE of 69.5% is achieved in HCE (Figure S9b). Moreover, the performance can be further enhanced by adopting LHCE. The voltage profiles consist of two charge plateaus at 0.70 V and 1.61 V, contributing to an accumulated capacity of 668 mAh g^{-1} with 70.8% ICE (Figure 4a, and dQ/dV curve in Figure S11). The improved specific capacity can be attributed to the higher ionic conductivity of LHCE than HCE, as discussed before. To quantify the K ion storage capacity of BP in BP/G composite, the ball-milled graphite electrodes are tested in LHCE (Figure S12a and b). It shows a low charge capacity of 83 mAh g^{-1} under 0.1 A g^{-1}, contributing only 2.5% capacity in the composite. Therefore, it can be calculated that about 814 mAh g^{-1} is contributed by BP, equivalent to 0.94 K ion per P atom participated in the alloying reaction. It is worth mentioning that the ball-milled BP electrodes without graphite cannot deliver such high specific capacity even in LHCE (Figure S12c and d). It emphasizes the synergistic effect of BP and graphite in achieving a high capacity and stable performance.

The well overlapped discharge-charge curves of BP/G electrode in HCE and LHCE suggest stable cyclic performances. BP/G electrode presents a capacity of 618 mAh g^{-1} with 92.7% retention after 70 cycles in LHCE under 0.1 A g^{-1} (Figure 4b), which outperforms the 399 mAh g^{-1} in HCE and is among the highest values achieved in P-based anodes (Table S1). Because of the high capacity and appropriate potential, the BP/G may greatly enhance the energy density of PIBs when coupled with a high-energy cathode. Noted that such a high capacity and stability could not be obtained in classic carbonate electrolytes. Noticeable capacity degradations are observed in conventional 1M KFSI/ECPC and highly concentrated 5M KFSI/ECPC electrolytes (Figure S13). Compared to HCE, much higher rate capacities are obtained in LHCE at increasing current density from 0.05 to 2.0 A g^{-1} (Figure 4c). A slight capacity increase at the initial cycles is observed at 0.05 A g^{-1} due possibly to the gradual activation of the large-sized particles. The CV scans at different rates are carried out to calculate the K ion diffusion coefficient according to the Randles-Sevcik equation (Figure S14). The results show the values in LHCE are about an order of magnitude higher than those in HCE (Figure 4d), indicating faster ion transfer in the former electrolyte. The electrochemical impedance spectroscopy (EIS) is performed to further study the kinetics behavior of the interphases formed in HCE and LHCE. As shown in Figure S15-S16 and Table S2-S3, close resistances of charge transfer (Rct) in HCE (5197 Ω) and LHCE (5106 Ω) are obtained for the cells at OCV state, and the values separately decrease to 628.2 and 627.4 Ω after building SEI. Nevertheless, the SEI (R_{SEI}) resistance in LHCE is much smaller than in HCE (134.6 *vs.* 756.2 Ω), confirming the faster charge transfer kinetics in the designed LHCE.

The long-term cycling of BP/G composite is conducted to evaluate the electrochemical stability (Figure 4e). Outstanding cyclic performances are obtained for BP/G when LHCE is employed, achieving a high reversible capacity of 342 and 291 mAh g^{-1} over 300 cycles under 0.3 and 0.5 A g^{-1}, respectively. We also examine the RP/G performance under the LHCE (Figure xx), which shows decent cyclic stability and confirms the benefits of LHCE. In contrast, there is apparent capacity degradation and fluctuation in the HCE after 200 cycles, dropping to 168 mAh g^{-1} in the 300th cycle under 0.3 A g^{-1}. Furthermore, the full cell performance in LHCE is demonstrated using the BP/G anode and a Prussian blue $K_xMnFe(CN)_6$ ($0 \leqslant x \leqslant 2$) cathode. The structure of $K_xMnFe(CN)_6$ has a monoclinic phase (ICSD#151697) (Figure S17a and the inset).[64] The $K_xMnFe(CN)_6$ half cell shows two discharge plateaus at about 4.0 and 3.9 V, leading to a cumulative capacity of xx mAh/g(Figure S17b-c). The full cell delivers a decent capacity of 82 mA g^{-1} (based on the total mass of anode and cathode) with a considerable rate capability at a current density up to 0.5 A g^{-1} (Figure S17d and e). A capacity of 77 mAh g^{-1} can be recovered and stabilized with a working potential of 3.01 V when the current density decreases to 0.025 A g^{-1}, giving rise to an energy density of 232 Wh kg^{-1}. This value is lower than the theoretical prediction due to the K ion consumption in the SEI formation, which may be resolved through pre-potassiation techniques, similar to that adopted in Li- and Na- ion batteries. We also couple the BP/G with a high-voltage $KVPO_4F$ cathode (Figure xx), demonstrating again the compability of as-prepared anode and electrolyte. Overall, these results indicate that the LHCE is fully compatible with the cathode.

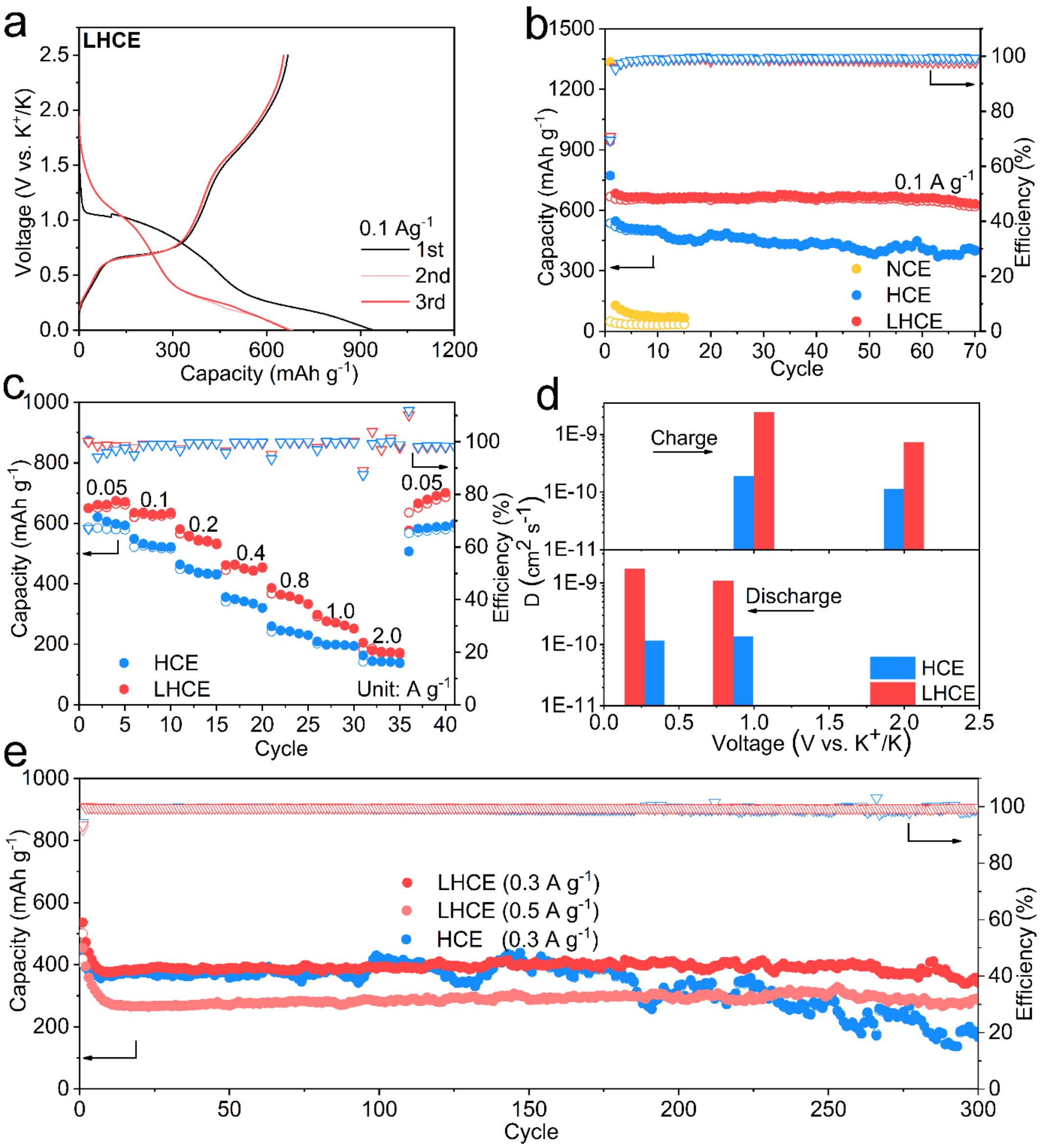

Figure 4 The electrochemical performances of BP/G. a) Voltage profiles under 0.1 A g^{-1} in LHCE; b) Cyclic performance under 0.1 A g^{-1} in NCE, HCE, and LHCE; c) rate capability in HCE and LHCE; d) Diffusion constant values derived from the CV profiles (Figure S14); e) Long-term cyclic performances in corresponding electrolytes.

To explore the underlying mechanism behind the electrolyte-induced enhancement, the SEI chemical compositions of the BP/G electrodes after cycling three times are investigated by XPS. As presented in the C1s and P2p spectra (Figure S18 and Figure 5a and b), the SEIs consist of C-

C (284.8 eV), C-OH (285.7 eV), C-O (286.7 eV), and P-O (around 133.3 eV) organic species, which are originated from the TMP decomposition. Other inorganic components are probed in F1s and S2p spectra, including K-F (683.6 eV), S-F (687.1 eV), (S=O)-N (168.3 eV), K_2SO_3 (166.1 eV) and K_2S (161.8 eV) species.[60, 65] In particular, the atomic concentrations of P and S elements presents significant differences in the three electrolytes. The SEI forming in NCE has the highest P content among the three but lower S content than those in HCE and LHCE (Figure 5c). The P and S elements in the SEI are mainly derived from the decomposition of TMP solvent and KFSI salt, respectively. That means the solvent decomposition is dominated in the low concentrated electrolyte, and more FSI^- anion reduction occurs in the high concentration counterpart. The preference for FSI^- anion decomposition is attributed to the lowest unoccupied molecular orbital (LUMO) shifting from solvent to anion because of the modified solvation structures of high concentration electrolytes .[49] Compared to the SEI in HCE, higher S content is found in the one under LHCE. The HFE additive enhances the interaction of cations and anions of the salt, and allows more FSI^- anions to participate in the K ion solvation sheath, which leads to rich anion-derived SEI.[66-67] Further exploring the deconvoluted spectra (Figure 5a-c), it shows that the SEI in LHCE has more rich (S=O)-N species but less amount of classic inorganic components such as KF (1.64 *vs*. 3.23%), K_2S (0.04% *vs*. 0.16%), and K_2SO_3 (0.25% *vs*. 0.71%) than those in HCE counterparts.

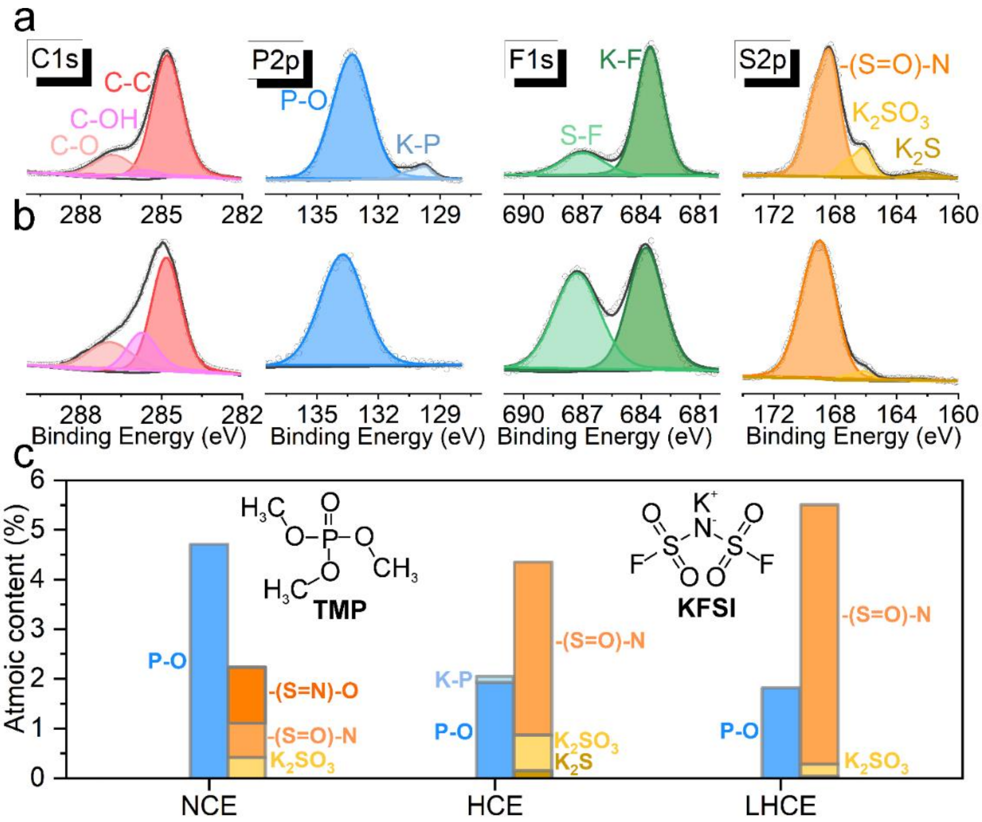

Figure 5. XPS Characterizations of BP/G electrodes after three cycles. C1s, P2p, F1s, and S2p spectra a) in HCE; b) LHCE; c) the atomic percentage of P and S elements in corresponding electrolytes.

The nanostructures of the SEIs are studied by TEM and energy-dispersive X-ray spectroscopy (EDS) mappings to examine the morphology and elemental distribution. In NCE (Figure S19), the discontinuous SEI with rough and ruptured morphology is observed on the particle surface, which cannot successfully protect the electrode, leading to the overwhelming electrolyte decomposition in the first discharge. The SEI with a thickness of 17.7 and 9.4 nm is formed in HCE (Figure S20a and b) and LHCE (Figure S20d and e), respectively. The thick SEI in HCE may undermine the rate capability. The C, O, S, F, K, and P elements show more uniform distributions in the LHCE than HCE (Figure S20c and f). Meanwhile, the electrodes after long-term cycling are also characterized to understand the discrepancy in cyclic stability. The thickness of the SEIs slightly increases to 22.3 for HCE and 12.2 nm for LHCE after 300 cycles (Figure 6a and c). It again confirms the robustness of SEI subject to the deformation, successfully passivating the electrode surface to prevent the continuous SEI growth. Such stable SEI is crucial in protecting the integrity of active particles and suppressing the parasitic reactions of electrolytes. More importantly, the SEI formed in LHCE maintains excellent structural homogeneity (Figure 6d) owing to the fast K ion transport. In comparison, the segregation phenomenon becomes more severe for the SEI in HCE, as evidenced in the elements mixed image (Figure 6b).

The elemental segregation in the SEI formed under HCE may explain the inferior stability compared to LHCE. To examine the speculation, the mechanical properties of SEIs in HCE and LHCE are probed by atomic force microscopy (AFM). Young's modulus (E) and elastic strain limit (εY) are the most widely used parameters for evaluating the SEI's mechanical stability, and the maximum elastic deformation energy (U) reflects their combined effect.[68] Elastic deformation is performed to determine the E in the 1st step AFM tests, while the SEI is intentionally fractured by applying a large indention force in the 2nd step to calculate εY. At least 90 points are measured to increase the accuracy of the test. A larger E of 1210 MPa is attained for the SEI build in HCE than the counterpart (810 MPa) in LHCE (Figure 6e). The reason lies in the presence of abundant KF (29 GPa), K_2SO_3 (45 GPa), and K_2S (19 GPa) components with high stiffness in HCE. Nevertheless, the SEI in LHCE shows higher εY than the one in HCE, attributed to the better homogeneity with reduced stress concentration. Combined the effects of E and ε_Y, the parameter U (proportional to $E \cdot \varepsilon_Y^5$, Equation 1), is used to appraise the mechanical stability of SEI. The SEI formed in LHCE shows a large U of 202.5 pJ, almost two times higher than in HCE (Figure 6f). The results indicate the better mechanical properties of the SEI in LHCE for accommodating the deformation to realize long lifespan BP/G electrode.

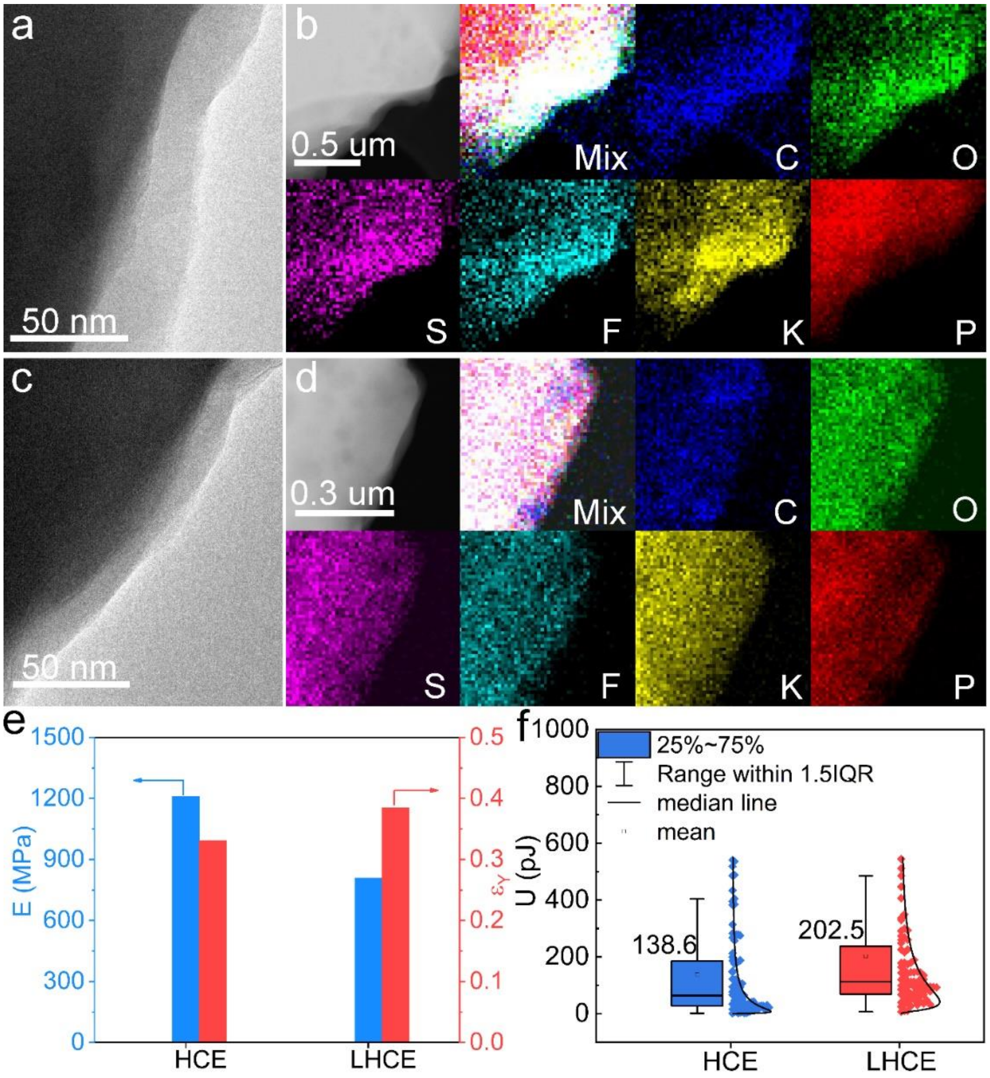

Figure 6 Morphologies and mechanical properties of the SEIs. The TEM, STEM images and EDS mapping after long-term cycling (300 cycles) in a, b) HCE and c, d) LHCE; e) Young's modulus (E) and elastic strain limit (ε_Y), and f) the maximum elastic deformation energy (U) of SEIs formed in these two electrolytes.

Conclusions

We prepare the BP/G electrode as advanced anodes in KIBs *via* a facile two-step ball milling approach. HEBM is adopted to transfer the RP into BP, which is mixed with graphite to obtain BP/G composite with a high BP loading of 80 wt.%. The electrode fails to deliver a decent reversible capacity in a standard concentration TMP-based electrolyte (1M). Increasing the concentration to 5M essentially boosts the reversibility, albeit the rate capability remains poor due to low ionic conductivity. Therefore, LHCE (KFSI/TMP/HFE with a molar ratio of 1: 1.7: 2) is designed to resolve the long-term stability and rate performance. The electrode presents a highly reversible and stable capacity of 342 mAh g^{-1} over 300 cycles under 0.3 A g^{-1} with the assistance of LHCE. Such an improvement roots in the enhanced ionic conductivity and the building of a robust SEI. We summarize the essential roles of SEI in governing the electrochemical behavior as follows: i) The absence of an effective SEI in NCE leads to negligible reversible capacity because of the copious electrotype decomposition. ii) The electrode shows a high reversible capacity in HCE but suffers from capacity degradation in long-term cycles. The inhomogeneous SEI with apparent elemental segregation reduces the yield strain. iii) The building of an inorganic component-rich SEI with uniform elemental distribution boosts the BP/G performance in the LHCE. On the one hand, the conformal SEI layer effectively prevents parasite reactions on the electrode surface. On the other hand, the homogenous SEI renders superb mechanical stability for accommodating deformation, as reflected by the large maximum elastic deformation energy. Lastly, we demonstrate that the electrolyte is fully compatible with the cathode, thus promoting the application of advanced KIBs with high-capacity BP anodes.

Experimental

Synthesis of RP, BP, RP/G, BP/G, K_4P_3 samples

The amorphous red phosphorous (RP) powder (Alfa Aeser, 98%) was purified before use. 2 g RP was washed by 200 mL boiling deionized water under the string and rinsed several times until the pH value turned neutral.[69] The purified RP powder was collected by centrifugation and dried at 70

˚C under vacuum. 1 g RP was sealed in the 100 mL jar under Ar atmosphere and ball milled (HEBM, SPEX 8000) for 1 hour to synthesize black phosphorous (BP). Afterward, 400 mg BP (80 wt.%) and 100 mg graphite (20 wt.%, KS6, MTI) were mixed by mechanical ball milling (QM-3SP2 planetary ball mill) for 48 hours under 360 rpm to prepare BP/G composite. RP/G composite was prepared following the same protocol by replacing the BP with RP. The ball-milled BP or graphite preparation was similar to BP/G composite, except without adding graphite or BP. The ball-milled samples were sealed under Ar atmosphere before ball milling, and the jar was open in the glovebox after the treatment. The K_4P_3 was synthesized by high-energy ball milling K metal (47 mg) and BP (28 mg) powder for 30 min under Ar atmosphere. To avoid oxidation, all the samples were stocked in the glovebox (O_2<0.1 ppm, H_2O<0.1 ppm).

Preparation of electrodes and electrolytes

A slurry was first prepared by hand grinding active materials (75 wt.%), super P (15 wt.%), polyacrylic acid (PAA, 10 wt.%) in N-methyl-2-pyrrolidone (NMP) in the glovebox. The slurry was cast on Cu foil and dried at 100 ˚C for 12 hours under vacuum in Buchi glass oven (B-585 Drying). All the electrodes were directly transferred into the glovebox in the Buchi glass oven without air contact. The tapes were chopped into ½ inch diameter electrodes with active mass loading of about 1 mg cm^{-2}. The $K_xMnFe(CN)_6$ cathode was synthesized following the previous report.[64] The cathode was prepared by mixing 70 wt.% $K_xMnFe(CN)_6$ and 30 wt.% super P, which is directly used in powder form electrode. The potassium bis(fluorosulfonyl)imide (KFSI, 98%) was purchased from Energy Chemical and 1,1,2,2-tetrafluoroethyl 2,2,2-trifluoroethyl ether (HFE, ⩾97%) was brought from Macklin. Trimethyl phosphate (TMP), ethylene carbonate (EC), propylene carbonate (PC) and dimethyl carbonate (DMC) were provided by DoDo Chem. All electrolyte salt and solvents were used without any purification. 1M KFSI/TMP (NCE), 5M

KFSI/TMP (HCE), KFSI/TMP/HFE with the molar ratio of 1:1.7:2 (LHCE), 1M KFSI/ECPC and 5M KFSI/ECPC were used as electrolytes. To prepare LHCE, the KFSI salt was first dissolved in TMP solvent under the string to form a transparent and clear solution, and then HFE was added and continuously stirred until the solution turned clear again.

Electrochemical measurements

CR2032 coin-type half-cells were assembled in the glovebox with K metal as the counter/reference electrode and one piece of glass fiber (GF/D, Whatman) as a separator. 75 uL of electrolytes were added to each cell. The galvanostatic tests were conducted on a LAND battery test system with the potential of 0-2.5V. Cyclic voltammetry (CV, 0-2.5V, 0.1-0.5 mV s^{-1}) was tested on Solartron Analytical 1400 electrochemical workstation. The electrochemical impedance spectroscopy (EIS, 100 kHz-0.1 HZ) was carried out on a Biologic SP150 electrochemical workstation with an amplitude of 5 mV. The full cell BP/G||$K_xMnFe(CN)_6$ was assembled with BP/G anode and $K_xMnFe(CN)_6$ cathode with cathode/anode mass ratio of about 6.

Materials characterizations

The X-ray diffraction (XRD) patterns were collected on X-ray Diffractometer (Rigaku SmartLab). Raman spectra were performed on Witec alpha 300 R with EL-CELL ECC-Opto-std test cell using 532 nm laser source. The morphologies of electrodes were observed by scanning electron microscope (SEM, Tescan VEGA3). X-ray photoelectron spectroscopy (XPS, Thermo Scientific Nexsa) was conducted to investigate the chemical compositions of solid electrolytes interphases (SEIs). The samples are sealed in a vacuum transfer holder to avoid air exposure. The nanostructures and EDS mappings of the SEIs were explored by transmission electron microscopy (TEM, JEOL JEM-2100F). Atomic force microscopy (AFM, Bruker Dimension Icon) was adopted to examine the mechanical properties of SEI in the glovebox. To avoid the possible interference from the binder, the electrode for AFM test was prepared by mixing BP/G (75 wt.%) with super P (25 wt.%), which were pre-cycled to build SEIs in HCE and LHCE. Detailed AFM tests and analyses could be found in the previous study.[68] The maximum elastic deformation energy is calculated by the following equation:

$$\mathrm{U} = \frac{8}{15}\left(\frac{4}{5}\pi\right)^5 \cdot r^3 \cdot (1-\nu^2)^4 \cdot E \cdot (\varepsilon_\mathrm{Y})^5 \quad \text{(Equation 1)}$$

where r is the radius of the rigid indenter (assumed as 1 μm), the ν is the SEI Poisson's ratio, and a typical value of 0.3 is used. E and ε_Y are corrected Young's modulus and yield strain after eliminating the substrate's interference.

ASSOCIATED CONTENT

Supporting Information: The following files are available free of charge.

The TEM of RP, STEM, EDS mappings and XPS of BP/G, EIS and Raman spectra of electrolytes and electrodes, SEM of cycled electrodes, electrochemical performances of ball-milled graphite and BP in LHCE and electrochemical performances of BP/G in carbonate-based electrolytes, CV rate curves of BP/G, EIS of BP/G at OCV state and after three times cycles, full cell performance, XPS and TEM of BP/G in NCE, TEM and EDS mappings of BP/G after cycling three times and tables of performance comparison and fitted impedances. (file type, i.e., PDF)

AUTHOR INFORMATION

Corresponding Author

*Biao Zhang, E-mail address: biao.ap.zhang@polyu.edu.hk

Author Contributions

All authors have given approval to the final version of the manuscript.

Funding Sources

General Research Fund (GRF) scheme of the Hong Kong Research Grants Council and the Hong Kong Polytechnic University.

ACKNOWLEDGMENT

This work was supported by the General Research Fund (GRF) scheme of the Hong Kong Research Grants Council (Project No. 15305219) and the Hong Kong Polytechnic University (ZVRP, ZVGH, 1-ZE30, and ZE2F). X. Du is grateful to Dr. Y. Gao for fruitful discussion on AFM test and Dr. X. Guo for assistance in TEM.

REFERENCES

1. Tian, Y.; Zeng, G.; Rutt, A.; Shi, T.; Kim, H.; Wang, J.; Koettgen, J.; Sun, Y.; Ouyang, B.; Chen, T., Promises and Challenges of Next-Generation “Beyond Li-ion” Batteries for Electric Vehicles and Grid Decarbonization. *Chemical reviews* **2020,** *121* (3), 1623-1669.
2. Kim, H.; Kim, J. C.; Bianchini, M.; Seo, D. H.; Rodriguez‐Garcia, J.; Ceder, G., Recent progress and perspective in electrode materials for K‐ion batteries. *Advanced Energy Materials* **2018,** *8* (9), 1702384.
3. Komaba, S.; Hasegawa, T.; Dahbi, M.; Kubota, K., Potassium intercalation into graphite to realize high-voltage/high-power potassium-ion batteries and potassium-ion capacitors. *Electrochemistry Communications* **2015,** *60*, 172-175.
4. Sun, Y.; Wang, H.; Wei, W.; Zheng, Y.; Tao, L.; Wang, Y.; Huang, M.; Shi, J.; Shi, Z.-C.; Mitlin, D., Sulfur-rich graphene nanoboxes with ultra-high potassiation capacity at fast charge: storage mechanisms and device performance. *ACS nano* **2020,** *15* (1), 1652-1665.
5. Tan, H.; Zhou, R.; Zhang, B., Understanding potassium ion storage mechanism in pitch-derived soft carbon and the consequence on cyclic stability. *Journal of Power Sources* **2021,** *506*, 230179.
6. Tan, H.; Du, X.; Zhou, R.; Hou, Z.; Zhang, B., Rational design of microstructure and interphase enables high-capacity and long-life carbon anodes for potassium ion batteries. *Carbon* **2021,** *176*, 383-389.
7. Zheng, J.; Yang, Y.; Fan, X.; Ji, G.; Ji, X.; Wang, H.; Hou, S.; Zachariah, M. R.; Wang, C., Extremely stable antimony–carbon composite anodes for potassium-ion batteries. *Energy & Environmental Science* **2019,** *12* (2), 615-623.
8. Huang, J.; Lin, X.; Tan, H.; Zhang, B., Bismuth microparticles as advanced anodes for potassium‐ion battery. *Advanced Energy Materials* **2018,** *8* (19), 1703496.
9. Du, X.; Gao, Y.; Zhang, B., Building Elastic Solid Electrolyte Interphases for Stabilizing Microsized Antimony Anodes in Potassium Ion Batteries. *Advanced Functional Materials* **2021**, 2102562.
10. Yi, Z.; Qian, Y.; Tian, J.; Shen, K.; Lin, N.; Qian, Y., Self-templating growth of Sb_2Se_3@C microtube: a convention-alloying-type anode material for enhanced K-ion batteries. *Journal of Materials Chemistry A* **2019,** *7* (19), 12283-12291.
11. Li, J.; Zhuang, N.; Xie, J.; Li, X.; Zhuo, W.; Wang, H.; Na, J. B.; Li, X.; Yamauchi, Y.; Mai, W., K‐Ion Storage Enhancement in Sb_2O_3/Reduced Graphene Oxide Using Ether‐Based Electrolyte. *Advanced Energy Materials* **2020,** *10* (5), 1903455.
12. Du, X.; Huang, J.; Guo, X.; Lin, X.; Huang, J.-Q.; Tan, H.; Zhu, Y.; Zhang, B., Preserved layered structure enables stable cyclic performance of MoS2 upon potassium insertion. *Chemistry of Materials* **2019,** *31* (21), 8801-8809.

13. Sui, X.; Huang, X.; Pu, H.; Wang, Y.; Chen, J., Tailoring MOF-derived porous carbon nanorods confined red phosphorous for superior potassium-ion storage. *Nano Energy* **2021,** *83*, 105797.

14. Zhang, W.; Pang, W. K.; Sencadas, V.; Guo, Z., Understanding high-energy-density Sn4P3 anodes for potassium-ion batteries. *Joule* **2018,** *2* (8), 1534-1547.

15. Huang, X.; Sui, X.; Ji, W.; Wang, Y.; Qu, D.; Chen, J., From phosphorus nanorods/C to yolk–shell P@ hollow C for potassium-ion batteries: high capacity with stable cycling performance. *Journal of Materials Chemistry A* **2020,** *8* (16), 7641-7646.

16. Yu, S.; Kim, S. O.; Kim, H. S.; Choi, W., Computational screening of anode materials for potassium‐ion batteries. *International Journal of Energy Research* **2019,** *43* (13), 7646-7654.

17. Wu, Y.; Huang, H. B.; Feng, Y.; Wu, Z. S.; Yu, Y., The promise and challenge of phosphorus‐based composites as anode materials for potassium‐ion batteries. *Advanced Materials* **2019,** *31* (50), 1901414.

18. Zhu, J.; Liu, Z.; Wang, W.; Yue, L.; Li, W.; Zhang, H.; Zhao, L.; Zheng, H.; Wang, J.; Li, Y., Green, Template-Less Synthesis of Honeycomb-like Porous Micron-Sized Red Phosphorus for High-Performance Lithium Storage. *ACS nano* **2021,** *15* (1), 1880-1892.

19. Zhu, Y.; Wen, Y.; Fan, X.; Gao, T.; Han, F.; Luo, C.; Liou, S.-C.; Wang, C., Red phosphorus–single-walled carbon nanotube composite as a superior anode for sodium ion batteries. *ACS nano* **2015,** *9* (3), 3254-3264.

20. Liu, Y.; Liu, Q.; Jian, C.; Cui, D.; Chen, M.; Li, Z.; Li, T.; Nilges, T.; He, K.; Jia, Z., Red-phosphorus-impregnated carbon nanofibers for sodium-ion batteries and liquefaction of red phosphorus. *Nature communications* **2020,** *11* (1), 1-8.

21. Fang, K.; Liu, D.; Xiang, X.; Zhu, X.; Tang, H.; Qu, D.; Xie, Z.; Li, J.; Qu, D., Air-stable red phosphorus anode for potassium/sodium-ion batteries enabled through dual-protection design. *Nano Energy* **2020,** *69*, 104451.

22. Qin, G.; Liu, Y.; Liu, F.; Sun, X.; Hou, L.; Liu, B.; Yuan, C., Magnetic Field Assisted Construction of Hollow Red P Nanospheres Confined in Hierarchical N‐Doped Carbon Nanosheets/Nanotubes 3D Framework for Efficient Potassium Storage. *Advanced Energy Materials* **2021,** *11* (4), 2003429.

23. Zhou, J.; Shi, Q.; Ullah, S.; Yang, X.; Bachmatiuk, A.; Yang, R.; Rummeli, M. H., Phosphorus‐Based Composites as Anode Materials for Advanced Alkali Metal Ion Batteries. *Advanced Functional Materials* **2020,** *30* (49), 2004648.

24. Ruan, J.; Mo, F.; Long, Z.; Song, Y.; Fang, F.; Sun, D.; Zheng, S., Tailor-Made Gives the Best Fits: Superior Na/K-Ion Storage Performance in Exclusively Confined Red Phosphorus System. *ACS nano* **2020,** *14* (9), 12222-12233.

25. Xiong, P.; Bai, P.; Tu, S.; Cheng, M.; Zhang, J.; Sun, J.; Xu, Y., Red Phosphorus Nanoparticle@ 3D Interconnected Carbon Nanosheet Framework Composite for Potassium‐Ion Battery Anodes. *Small* **2018,** *14* (33), 1802140.

26. Chang, W. C.; Wu, J. H.; Chen, K. T.; Tuan, H. Y., Red Phosphorus Potassium‐Ion Battery Anodes. *Advanced Science* **2019,** *6* (9), 1801354.

27. Liu, D.; Huang, X.; Qu, D.; Zheng, D.; Wang, G.; Harris, J.; Si, J.; Ding, T.; Chen, J.; Qu, D., Confined phosphorus in carbon nanotube-backboned mesoporous carbon as superior anode material for sodium/potassium-ion batteries. *Nano Energy* **2018,** *52*, 1-10.

28. Xiao, W.; Li, X.; Cao, B.; Huang, G.; Xie, C.; Qin, J.; Yang, H.; Wang, J.; Sun, X., Constructing high-rate and long-life phosphorus/carbon anodes for potassium-ion batteries through rational nanoconfinement. *Nano Energy* **2021,** *83*, 105772.

29. Zhang, S.; Liu, C.; Wang, H.; Wang, H.; Sun, J.; Zhang, Y.; Han, X.; Cao, Y.; Liu, S.; Sun, J., A Covalent P–C Bond Stabilizes Red Phosphorus in an Engineered Carbon Host for High-Performance Lithium-Ion Battery Anodes. *ACS nano* **2021,** *15* (2), 3365-3375.

30. Gusmao, R.; Sofer, Z.; Pumera, M., Black phosphorus rediscovered: from bulk material to monolayers. *Angewandte Chemie International Edition* **2017,** *56* (28), 8052-8072.

31. Ren, X.; Lian, P.; Xie, D.; Yang, Y.; Mei, Y.; Huang, X.; Wang, Z.; Yin, X., Properties, preparation and application of black phosphorus/phosphorene for energy storage: a review. *Journal of Materials Science* **2017,** *52* (17), 10364-10386.

32. Liu, H.; Du, Y.; Deng, Y.; Peide, D. Y., Semiconducting black phosphorus: synthesis, transport properties and electronic applications. *Chemical Society Reviews* **2015,** *44* (9), 2732-2743.

33. Xu, G.-L.; Chen, Z.; Zhong, G.-M.; Liu, Y.; Yang, Y.; Ma, T.; Ren, Y.; Zuo, X.; Wu, X.-H.; Zhang, X., Nanostructured black phosphorus/Ketjenblack–multiwalled carbon nanotubes composite as high performance anode material for sodium-ion batteries. *Nano letters* **2016,** *16* (6), 3955-3965.

34. Jin, H.; Xin, S.; Chuang, C.; Li, W.; Wang, H.; Zhu, J.; Xie, H.; Zhang, T.; Wan, Y.; Qi, Z.; Yan, W.; Lu, Y.-R.; Chan, T.-S.; Wu, X.; Goodenough, J. B.; Ji, H.; Duan, X., Black phosphorus composites with engineered interfaces for high-rate high-capacity lithium storage. *Science* **2020,** *370* (6513), 192-197.

35. Ferrara, C.; Vigo, E.; Albini, B.; Galinetto, P.; Milanese, C.; Tealdi, C.; Quartarone, E.; Passerini, S.; Mustarelli, P., Efficiency and quality issues in the production of black phosphorus by mechanochemical synthesis: a multi-technique approach. *ACS Applied Energy Materials* **2019,** *2* (4), 2794-2802.

36. Sultana, I.; Rahman, M. M.; Ramireddy, T.; Chen, Y.; Glushenkov, A. M., High capacity potassium-ion battery anodes based on black phosphorus. *Journal of Materials Chemistry A* **2017,** *5* (45), 23506-23512.

37. Jin, H.; Wang, H.; Qi, Z.; Bin, D. S.; Zhang, T.; Wan, Y.; Chen, J.; Chuang, C.; Lu, Y. R.; Chan, T. S., A Black Phosphorus ‐ Graphite Composite Anode for Li ‐ /Na ‐ /K ‐ Ion Batteries. *Angewandte Chemie* **2020,** *132* (6), 2338-2342.

38. Capone, I.; Aspinall, J.; Darnbrough, E.; Zhao, Y.; Wi, T.-U.; Lee, H.-W.; Pasta, M., Electrochemo-Mechanical Properties of Red Phosphorus Anodes in Lithium, Sodium, and Potassium Ion Batteries. *Matter* **2020,** *3* (6), 2012-2028.

39. Yang, F.; Hao, J.; Long, J.; Liu, S.; Zheng, T.; Lie, W.; Chen, J.; Guo, Z., Achieving High ‐ Performance Metal Phosphide Anode for Potassium Ion Batteries via Concentrated Electrolyte Chemistry. *Advanced Energy Materials* **2021,** *11* (6), 2003346.

40. Zhou, L.; Cao, Z.; Zhang, J.; Cheng, H.; Liu, G.; Park, G. T.; Cavallo, L.; Wang, L.; Alshareef, H. N.; Sun, Y. K., Electrolyte ‐ Mediated Stabilization of High ‐ Capacity Micro ‐ Sized Antimony Anodes for Potassium ‐ Ion Batteries. *Advanced Materials* **2021,** *33* (8), 2005993.

41. Li, X.; Ou, X.; Tang, Y., 6.0 V high ‐ voltage and concentrated electrolyte toward high energy density K ‐ based dual ‐ graphite battery. *Advanced Energy Materials* **2020,** *10* (41), 2002567.

42. Li, M.; Wang, C.; Chen, Z.; Xu, K.; Lu, J., New concepts in electrolytes. *Chemical reviews* **2020,** *120* (14), 6783-6819.

43. Liu, S.; Mao, J.; Zhang, L.; Pang, W. K.; Du, A.; Guo, Z., Manipulating the Solvation Structure of Nonflammable Electrolyte and Interface to Enable Unprecedented Stability of

Graphite Anodes beyond 2 Years for Safe Potassium‐Ion Batteries. *Advanced Materials* **2021,** *33* (1), 2006313.

44. Jiang, L. L.; Yan, C.; Yao, Y. X.; Cai, W.; Huang, J. Q.; Zhang, Q., Inhibiting Solvent Co-Intercalation in a Graphite Anode by a Localized High-Concentration Electrolyte in Fast-Charging Batteries. *Angew Chem Int Ed Engl* **2021,** *60* (7), 3402-3406.

45. Ren, X.; Zou, L.; Cao, X.; Engelhard, M. H.; Liu, W.; Burton, S. D.; Lee, H.; Niu, C.; Matthews, B. E.; Zhu, Z.; Wang, C.; Arey, B. W.; Xiao, J.; Liu, J.; Zhang, J.-G.; Xu, W., Enabling High-Voltage Lithium-Metal Batteries under Practical Conditions. *Joule* **2019,** *3* (7), 1662-1676.

46. Jia, H.; Zou, L.; Gao, P.; Cao, X.; Zhao, W.; He, Y.; Engelhard, M. H.; Burton, S. D.; Wang, H.; Ren, X.; Li, Q.; Yi, R.; Zhang, X.; Wang, C.; Xu, Z.; Li, X.; Zhang, J. G.; Xu, W., High‐Performance Silicon Anodes Enabled By Nonflammable Localized High‐Concentration Electrolytes. *Advanced Energy Materials* **2019,** *9* (31).

47. Jin, Y.; Xu, Y.; Le, P. M. L.; Vo, T. D.; Zhou, Q.; Qi, X.; Engelhard, M. H.; Matthews, B. E.; Jia, H.; Nie, Z.; Niu, C.; Wang, C.; Hu, Y.; Pan, H.; Zhang, J.-G., Highly Reversible Sodium Ion Batteries Enabled by Stable Electrolyte-Electrode Interphases. *ACS Energy Letters* **2020,** *5* (10), 3212-3220.

48. Zheng, J.; Chen, S.; Zhao, W.; Song, J.; Engelhard, M. H.; Zhang, J.-G., Extremely Stable Sodium Metal Batteries Enabled by Localized High-Concentration Electrolytes. *ACS Energy Letters* **2018,** *3* (2), 315-321.

49. Cao, X.; Jia, H.; Xu, W.; Zhang, J.-G., Localized High-Concentration Electrolytes for Lithium Batteries. *Journal of the Electrochemical Society* **2021,** *168* (1), 010522.

50. Perez Beltran, S.; Cao, X.; Zhang, J.-G.; Balbuena, P. B., Localized High Concentration Electrolytes for High Voltage Lithium–Metal Batteries: Correlation between the Electrolyte Composition and Its Reductive/Oxidative Stability. *Chemistry of Materials* **2020,** *32* (14), 5973-5984.

51. Piao, N.; Ji, X.; Xu, H.; Fan, X.; Chen, L.; Liu, S.; Garaga, M. N.; Greenbaum, S. G.; Wang, L.; Wang, C.; He, X., Countersolvent Electrolytes for Lithium‐Metal Batteries. *Advanced Energy Materials* **2020,** *10* (10).

52. Qin, L.; Xiao, N.; Zheng, J.; Lei, Y.; Zhai, D.; Wu, Y., Localized High‐Concentration Electrolytes Boost Potassium Storage in High‐Loading Graphite. *Advanced Energy Materials* **2019,** *9* (44).

53. Liu, X.; Zheng, X.; Dai, Y.; Wu, W.; Huang, Y.; Fu, H.; Huang, Y.; Luo, W., Fluoride‐Rich Solid‐Electrolyte‐Interface Enabling Stable Sodium Metal Batteries in High‐Safe Electrolytes. *Advanced Functional Materials* **2021**, 2103522.

54. Ou, X.; Li, J.; Tong, X.; Zhang, G.; Tang, Y., Highly Concentrated and Nonflammable Electrolyte for High Energy Density K-Based Dual-Ion Battery. *ACS Applied Energy Materials* **2020,** *3* (10), 10202-10208.

55. Zaug, J. M.; Soper, A. K.; Clark, S. M., Pressure-dependent structures of amorphous red phosphorus and the origin of the first sharp diffraction peaks. *Nature materials* **2008,** *7* (11), 890-899.

56. Liu, F.; Shi, R.; Wang, Z.; Weng, Y.; Che, C. M.; Chen, Y., Direct Z-Scheme Hetero-phase Junction of Black/Red Phosphorus for Photocatalytic Water Splitting. *Angew Chem Int Ed Engl* **2019,** *58* (34), 11791-11795.

57. Chhetry, A.; Sharma, S.; Barman, S. C.; Yoon, H.; Ko, S.; Park, C.; Yoon, S.; Kim, H.; Park, J. Y., Black Phosphorus@Laser-Engraved Graphene Heterostructure-Based Temperature-

Strain Hybridized Sensor for Electronic-Skin Applications. *Advanced Functional Materials* **2020,** *31* (10).

58. Xing, T.; Li, L. H.; Hou, L.; Hu, X.; Zhou, S.; Peter, R.; Petravic, M.; Chen, Y., Disorder in ball-milled graphite revealed by Raman spectroscopy. *Carbon* **2013,** *57*, 515-519.

59. Sun, J.; Zheng, G.; Lee, H.-W.; Liu, N.; Wang, H.; Yao, H.; Yang, W.; Cui, Y., Formation of stable phosphorus–carbon bond for enhanced performance in black phosphorus nanoparticle–graphite composite battery anodes. *Nano letters* **2014,** *14* (8), 4573-4580.

60. Zeng, G.; Xiong, S.; Qian, Y.; Ci, L.; Feng, J., Non-Flammable Phosphate Electrolyte with High Salt-to-Solvent Ratios for Safe Potassium-Ion Battery. *Journal of The Electrochemical Society* **2019,** *166* (6), A1217-A1222.

61. Ren, X.; Chen, S.; Lee, H.; Mei, D.; Engelhard, M. H.; Burton, S. D.; Zhao, W.; Zheng, J.; Li, Q.; Ding, M. S.; Schroeder, M.; Alvarado, J.; Xu, K.; Meng, Y. S.; Liu, J.; Zhang, J.-G.; Xu, W., Localized High-Concentration Sulfone Electrolytes for High-Efficiency Lithium-Metal Batteries. *Chem* **2018,** *4* (8), 1877-1892.

62. Wu, Y.; Hu, S.; Xu, R.; Wang, J.; Peng, Z.; Zhang, Q.; Yu, Y., Boosting potassium-ion battery performance by encapsulating red phosphorus in free-standing nitrogen-doped porous hollow carbon nanofibers. *Nano letters* **2019,** *19* (2), 1351-1358.

63. Abellan, G.; Neiss, C.; Lloret, V.; Wild, S.; Chacon-Torres, J. C.; Werbach, K.; Fedi, F.; Shiozawa, H.; Gorling, A.; Peterlik, H.; Pichler, T.; Hauke, F.; Hirsch, A., Exploring the Formation of Black Phosphorus Intercalation Compounds with Alkali Metals. *Angew Chem Int Ed Engl* **2017,** *56* (48), 15267-15273.

64. Xue, L.; Li, Y.; Gao, H.; Zhou, W.; Lu, X.; Kaveevivitchai, W.; Manthiram, A.; Goodenough, J. B., Low-Cost High-Energy Potassium Cathode. *J Am Chem Soc* **2017,** *139* (6), 2164-2167.

65. Jiang, X.; Liu, X.; Zeng, Z.; Xiao, L.; Ai, X.; Yang, H.; Cao, Y., A Nonflammable Na+

-Based Dual-Carbon Battery with Low-Cost, High Voltage, and Long Cycle Life. *Advanced Energy Materials* **2018,** *8* (36).

66. Ding, J. F.; Xu, R.; Yao, N.; Chen, X.; Xiao, Y.; Yao, Y. X.; Yan, C.; Xie, J.; Huang, J. Q., Non-Solvating and Low-Dielectricity Cosolvent for Anion-Derived Solid Electrolyte Interphases in Lithium Metal Batteries. *Angew Chem Int Ed Engl* **2021,** *60* (20), 11442-11447.

67. Yan, C.; Jiang, L. L.; Yao, Y. X.; Lu, Y.; Huang, J. Q.; Zhang, Q., Nucleation and Growth Mechanism of Anion-Derived Solid Electrolyte Interphase in Rechargeable Batteries. *Angew Chem Int Ed Engl* **2021,** *60* (15), 8521-8525.

68. Gao, Y.; Du, X.; Hou, Z.; Shen, X.; Mai, Y.-W.; Tarascon, J.-M.; Zhang, B., Unraveling the mechanical origin of stable solid electrolyte interphase. *Joule* **2021,** *5* (7), 1860-1872.

69. Smith, J. B.; Hagaman, D.; Ji, H. F., Growth of 2D black phosphorus film from chemical vapor deposition. *Nanotechnology* **2016,** *27* (21), 215602.